A depth-averaged electrokinetic flow model for shallow microchannels

HAO LIN[1]†, BRIAN D. STOREY[2] AND JUAN G. SANTIAGO[1]

[1]Mechanical Engineering Department, Stanford University, Stanford, CA 94305, USA
[2]Franklin W. Olin College of Engineering, Needham, MA 02492, USA

Electrokinetic flows with heterogeneous conductivity configuration occur widely in microfluidic applications such as sample stacking and multidimensional assays. Electromechanical coupling in these flows may lead to complex flow phenomena, such as sample dispersion due to electro-osmotic velocity mismatch, and electrokinetic instability (EKI). In this work we develop a generalized electrokinetic model suitable for the study of microchannel flows with conductivity gradients and shallow-channel geometry. An asymptotic analysis is performed with the channel depth-to-width ratio as a smallness parameter, and the three-dimensional equations are reduced to a set of depth-averaged equations governing in-plane flow dynamics. The momentum equation uses a Darcy–Brinkman–Forchheimer-type formulation, and the convective–diffusive transport of the conductivity field in the depth direction manifests itself as a dispersion effect on the in-plane conductivity field. The validity of the model is assessed by comparing the numerical results with full three-dimensional direct numerical simulations, and experimental data. The depth-averaged equations provide the accuracy of three-dimensional modelling with a convenient two-dimensional equation set applicable to a wide class of microfluidic devices.

1. Introduction

Electrokinetic flows with conductivity gradients occur in a wide range of microfluidic applications including sample stacking, multidimensional assays and assays with poorly controlled sample chemistry (Burgi & Chien 1991; Herr *et al.* 2003). Coupling between electrostatic and mechanical forces in these flows may sometimes lead to complex flow phenomena including sample dispersion due to electro-osmotic flow mismatch and electrokinetic instability (EKI). In earlier work (Lin *et al.* 2004; Chen *et al.* 2005; Storey *et al.* 2005; Bharadwaj & Santiago 2005), we and our co-authors studied these physical phenomena, and our results provided good agreement with experimental data (Oddy, Santiago & Mikkelsen 2001; Chen & Santiago 2002).

A common characteristic of the systems we have previously studied is that flow channels were all 'shallow' with depth dimensions (z) small compared with channel widths (y) or lengths (x). Shallow-channel geometries are common in electrokinetic microfluidic devices as they are typically fabricated in glass or silica using photolithography and wet etching (Reyes *et al.* 2002). In Lin *et al.* (2004) and within the context of EKI study, we demonstrated that a purely two-dimensional

---

† Present Address: Mechanical and Aerospace Engineering Department, Rutgers, The State University of New Jersey, USA. hlin@jove.rutgers.edu.

model was insufficient in modelling complex electrokinetic flows. A three-dimensional analysis was required in order to make accurate quantitative predictions of the stability threshold observed in experiments. In Chen *et al.* (2005) and Storey *et al.* (2005), we proposed various linear or lower-order depth-averaged models for the study of both convective and absolute EKI. In these models, the full three-dimensional equations were reduced to sets of effective two-dimensional equations through depth-averaging. The advantage of this approach is that more complex flow physics can be captured without resorting to expensive three-dimensional computations.

In this paper, we extend and complete the ideas first developed in Chen *et al.* (2005) and Storey *et al.* (2005). We aim to develop a generalized nonlinear depth-averaged model suitable for the study of electrokinetic microchannel flows in thin channels. We accomplish this through a complete asymptotic analysis based on the small channel aspect ratio. Similar solution approaches can be found in cylindrical geometries. For example, Ghosal (2003) employed area averaging in the context of capillary-zone electrophoresis. We will derive a Darcy–Brinkman–Forchheimer-type of momentum equation in the context of electrokinetic flow, and we shall also present a generalized two-dimensional Taylor dispersion equation. We evaluate the accuracy of our model by comparing the model results with full three-dimensional direct numerical simulations (DNS) and experimental data.

2. Formulation

In Lin *et al.* (2004), we developed a set of governing equations suitable for the study of general electrokinetic flows in microchannels, with specific applications to EKI. The governing equations begin with the conservation of mass for a two-species symmetric electrolyte solution, Poisson's equation for the electric field, the conservation of mass for an incompressible liquid, and the conservation of momentum including the body force due to an electric field acting on charged fluid (Probstein 1994). These complete equations are simplified when we make use of three assumptions:

(*a*) that the charge relaxes instantaneously;

(*b*) that in the fluid bulk, the difference in cationic and anionic concentrations is small compared to the background concentration (electroneutrality); and

(*c*) that the electric double layers that form near the channel walls are very small compared to the system size.

Assumption (*a*) holds when the charge relaxation time, ϵ/σ, is much shorter than the flow times in the system. Here ϵ and σ are the permittivity and electrical conductivity, respectively. Even when the salt concentration is dilute ($\sim 30\,\mu\text{M}$) and the conductivity is low, the charge relaxation time is of the order of $1\,\mu\text{s}$. Assumption (*b*) holds when the dimensionless parameter $\epsilon E_0/F C_0 d \ll 1$. Here, E_0 is the magnitude of the applied field, F is Faraday's constant, C_0 is the background ion concentration, and d is the channel dimension. Typical of our applications, this number is of the order of 10^{-5}. Finally, assumption (*c*) holds when $\lambda_D/d \ll 1$, where λ_D is the Debye length. Typical values for λ_D are 50 nm or less and the smallest channel dimensions are $10\,\mu\text{m}$ or greater.

Upon making these assumptions, we arrive at the governing equations which we will use as our starting point (see Lin *et al.* 2004 for details). Under the above restrictions, the (dimensional) governing equations are:

$$\frac{\partial \sigma}{\partial t} + \boldsymbol{v} \cdot \boldsymbol{\nabla}\sigma = D\nabla^2\sigma, \tag{2.1}$$

$$\boldsymbol{\nabla} \cdot (\sigma \boldsymbol{\nabla}\Phi) = 0, \tag{2.2}$$

$$\epsilon \nabla^2 \Phi = -\rho_E, \tag{2.3}$$

$$\nabla \cdot \boldsymbol{v} = 0, \tag{2.4}$$

$$\rho \left(\frac{\partial \boldsymbol{v}}{\partial t} + \boldsymbol{v} \cdot \nabla \boldsymbol{v} \right) = -\nabla p + \mu \nabla^2 \boldsymbol{v} - \rho_E \nabla \Phi. \tag{2.5}$$

Here D is the diffusivity of the conductivity field which is derived from those of the composing ion species, $\boldsymbol{v} = (u, v, w)$ is the velocity field, Φ is the electric potential, ρ_E is the charge density, ρ is the buffer liquid density (which can be assumed to be that of water for dilute aqueous buffers), p is the pressure, and μ is the liquid viscosity. Equations (2.1)–(2.5) represent the conservation of conductivity, current continuity, Poisson's equation for the electric potential, conservation of mass for an incompressible fluid, and conservation of momentum, respectively. Since we are assuming a symmetric binary electrolyte (such as potassium chloride KCl) it is convenient to use electrical conductivity and charge density as variables as opposed to tracking molar concentration of individual ionic species. Note that the electrical body force term ($-\rho_E \nabla \Phi$ in (2.5)) is retained even outside the electric double layers, i.e. in the fluid bulk. The electrical body force is present when the electric field is not orthogonal to the electrical conductivity gradient (Hoburg & Melcher 1976; Lin *et al.* 2004; Chen *et al.* 2005).

These equations are subject to the following boundary conditions at channel walls:

$$\nabla \sigma \cdot \boldsymbol{n} = 0, \tag{2.6}$$

$$\nabla \Phi \cdot \boldsymbol{n} = 0, \tag{2.7}$$

$$\boldsymbol{v} \cdot \boldsymbol{n} = 0, \tag{2.8}$$

$$\boldsymbol{v} \cdot \boldsymbol{t} = -\frac{\epsilon \zeta}{\mu} \nabla \Phi \cdot \boldsymbol{t}, \tag{2.9}$$

where $\boldsymbol{n}$ and $\boldsymbol{t}$ are the normal and tangent vectors attached to a solid surface, respectively, ζ is a wall zeta potential, and (2.9) is the Helmholtz–Smoluchowski formula for electro-osmotic slip velocity. The typical value of ζ for a millimolar electrolyte with pH $\geqslant 7$ and a glass surface is about -0.1 V (Probstein 1994). It is well-known that the zeta potential depends upon the local ionic concentration which can lead to sample dispersion in applications such as field amplified sample stacking (Burgi & Chien 1991).

It is important to note that the governing equations are strictly only valid for the fluid outside the thin electric double layers which form near the channel walls. Further, the boundary conditions are strictly applied at the outer interface of the electric double layers, not at the channel walls. However, in our applications, the electric double-layer thickness is typically three orders of magnitude smaller than the smallest channel dimension, $\lambda_D/d \sim 10^{-3}$. In this case, we may simply model the electric double layers through the effective 'slip' boundary conditions, equation (2.9) (Probstein 1994).

2.1. *Non-dimensionalization and scaling analysis*

We non-dimensionalize (2.1)–(2.9) using the following scales:

$$\left. \begin{array}{l} [x, y] = H, \quad [z] = d, \quad [\Phi] = \Phi_o = E_o H, \quad [\sigma] = \sigma_o, \quad [u, v] = U_{ev} \equiv \dfrac{\epsilon E_o^2 d^2}{\mu H}, \\[3mm] [w] = \dfrac{U_{ev} d}{H}, \quad [t] = t_o = \dfrac{H}{U_{ev}}, \quad [p] = \dfrac{\mu U_{ev} H}{d^2}, \quad [\zeta] = \zeta_o. \end{array} \right\} \tag{2.10}$$

Here, H is a half-width (in the y-direction), and d is the half-depth (z-direction) of the channel. The characteristic field E_o is taken to be the value of the applied field, σ_o is the characteristic conductivity of the electrolyte solution, and ζ_o is a reference zeta potential. The scale for the horizontal velocities, the so-called electroviscous velocity U_{ev}, is set such that the viscous force balances the electrical body force in (2.5) (Hoburg & Melcher 1976; Lin *et al.* 2004; Chen *et al.* 2005; Storey *et al.* 2005). Note that the choice of the velocity scale is not unique. In certain applications where velocity gradients due to electro-osmosis dominate over those due to electroviscous forces, the appropriate scale may be $\Delta U_{eo} = U_{eo,2} - U_{eo,1}$, where $U_{eo,2}$ and $U_{eo,1}$ are, respectively, the maximum and minimum values of electro-osmotic velocity. However, the choice of the dispersion velocity scale does not affect our analysis. We defer further discussion to §3.3. We have also set the pressure gradient to be of the same order of magnitude as the viscous and electric body forces. Finally, the scale for the vertical velocity w is set such that all three terms in the continuity equation (see (2.14) below) are of the same order. Owing to the assumed shallow channel depth, we further define a smallness parameter to be

$$\delta \equiv \frac{d}{H}. \tag{2.11}$$

After non-dimensionalization, we obtain the following set of dimensionless equations:

$$Pe_d\delta \left(\frac{\partial \sigma}{\partial t} + \boldsymbol{v} \cdot \nabla \sigma \right) = \frac{\partial^2 \sigma}{\partial z^2} + \delta^2 \nabla_H^2 \sigma, \tag{2.12}$$

$$\delta^2 \nabla_H \cdot (\sigma \nabla_H \Phi) + \frac{\partial}{\partial z} \left(\sigma \frac{\partial \Phi}{\partial z} \right) = 0, \tag{2.13}$$

$$\frac{\partial u}{\partial x} + \frac{\partial v}{\partial y} + \frac{\partial w}{\partial z} = 0, \tag{2.14}$$

$$Re_d\delta \left(\frac{\partial \boldsymbol{u}}{\partial t} + \boldsymbol{v} \cdot \nabla \boldsymbol{u} \right) = -\nabla_H p + \frac{\partial^2 \boldsymbol{u}}{\partial z^2} + \delta^2 \nabla_H^2 \boldsymbol{u} + \left(\nabla_H^2 \Phi + \frac{1}{\delta^2} \frac{\partial^2 \Phi}{\partial z^2} \right) \nabla_H \Phi, \tag{2.15}$$

$$Re_d\delta^3 \left(\frac{\partial w}{\partial t} + \boldsymbol{v} \cdot \nabla w \right) = -\frac{\partial p}{\partial z} + \delta^2 \frac{\partial^2 w}{\partial z^2} + \delta^4 \nabla_H^2 w + \left(\nabla_H^2 \Phi + \frac{1}{\delta^2} \frac{\partial^2 \Phi}{\partial z^2} \right) \frac{\partial \Phi}{\partial z}. \tag{2.16}$$

For convenience, we have denoted the horizontal velocity vector as $\boldsymbol{u} \equiv (u, v)$ to distinguish it from the three-dimensional velocity vector $\boldsymbol{v}$. We also denote a two-dimensional in-plane gradient as

$$\nabla_H \equiv \left(\frac{\partial}{\partial x}, \frac{\partial}{\partial y} \right). \tag{2.17}$$

Different from our presentation in Lin *et al.* (2004), the Péclet and Reynolds numbers are now more appropriately based on the small depth scale d, that is

$$Pe_d \equiv \frac{U_{ev}d}{D}, \qquad Re_d \equiv \frac{\rho U_{ev}d}{\mu}. \tag{2.18}$$

The boundary conditions have the same forms except for the tangential velocities, i.e.

$$\boldsymbol{v} \cdot \boldsymbol{t} = -\frac{1}{R_v} \zeta \nabla \Phi \cdot \boldsymbol{t}, \tag{2.19}$$

where the dimensionless group

$$R_v \equiv -\frac{E_o d^2}{\zeta_o H} \tag{2.20}$$

denotes the ratio of electroviscous to electro-osmotic velocities.

For our numerical computations, we adopt an empirical correlation for the non-dimensional zeta potential (Yao *et al.* 2003),

$$\zeta(\sigma) = \sigma^{-n}. \tag{2.21}$$

In this relation, we have chosen a zeta potential scale ζ_o to be that at the reference conductivity σ_o. For the power index, we adopt $n \approx 0.33$ based on experimental data (Yao *et al.* 2003; Sadr *et al.* 2004). (For a channel surface of fixed charge, the theoretical value is $n = -1/2$ based on solutions to the Poisson–Boltzmann equations (Probstein 1994).) We emphasize that (2.21) is an experimentally validated approximation and chosen as an example to compute electro-osmotic velocity in typical glass or silicon microchannels, which facilitates comparison with experiments. However, our analysis does not depend on the specific form of zeta potential. Our results can be used with any zeta potential model in so far as the resulting electro-osmotic velocity at the top ($z = +1$) and bottom ($z = -1$) of the microchannels are equal at every in-plane (x, y) location. Further discussions on this latter constraint, as well as the validity of (2.21) are presented in Appendix B. In the following and without losing generality, we shall simply write the boundary condition (2.19) as

$$\boldsymbol{v} \cdot \boldsymbol{t} = -\frac{1}{R_v} \zeta \nabla \Phi \equiv \boldsymbol{u}_{eo}, \tag{2.22}$$

where $\boldsymbol{u}_{eo}$ denotes the local electro-osmotic velocity, and we shall assume $\boldsymbol{u}_{eo}(x, y, z = +1) = \boldsymbol{u}_{eo}(x, y, z = -1)$.

We perform asymptotic analysis on the system of equations (2.12)–(2.16), assuming that $\delta \ll 1$. We expand our variables as

$$f = f_0 + \delta f_1 + \delta^2 f_2 + \cdots, \tag{2.23}$$

and substitute them into the governing equations for balances on the same order. Our goal is to construct a set of two-dimensional depth-averaged equations with first-order (second-order in the momentum equation) consistency in δ. Note that in the governing equations (2.12)–(2.16) there are two other dimensionless parameters, namely, Pe_d and Re_d. In order for the asymptotic analysis to be valid, $Re_d \delta \ll 1$ and $Pe_d \delta \ll 1$ must be satisfied. These constraints suggest that both the viscous and molecular diffusion time scales are much smaller when compared with the convective time scale. Further discussions on these constraints are deferred to §3.3.

2.2. *Flow field*

The flow-field analysis follows a Darcy–Brinkman–Forchheimer (DBF) approach, in which we include both inertia and in-plane viscous diffusion effects. The DBF model has been extensively adopted to study flows in porous media and biological tissues (see for example, Vafai & Tien 1981; Liu & Masliyah 1996; Khaled & Vafai 2003), and here we extend the model to electrokinetic applications and demonstrate its

superiority over the simpler lower-order Darcy equation (see (7) in Khaled & Vafai, and (2.74) below).

The δ^0-order balance of (2.14), (2.15) and (2.16) gives

$$\nabla_H \cdot \boldsymbol{u}_0 + \frac{\partial w_0}{\partial z} = 0, \tag{2.24}$$

$$0 = -\nabla_H p_0 + \frac{\partial^2 \boldsymbol{u}_0}{\partial z^2} + \nabla_H^2 \Phi_0 \nabla_H \Phi_0, \tag{2.25}$$

$$0 = -\frac{\partial p_0}{\partial z}. \tag{2.26}$$

In deriving these equations, special attention should be paid to the charge density terms $(1/\delta^2)\partial^2 \Phi/\partial z^2$ in (2.15) and (2.16). The multiplier $1/\delta^2$ suggests that a slight vertical variations in Φ can generate a large effect. However, our analysis (presented in §2.4 and Appendix A) shows that

$$\Phi_0 = \Phi_0(x, y, t), \quad \Phi_1 = \Phi_1(x, y, t), \quad \Phi_2 = \Phi_2(x, y, t), \tag{2.27}$$

and the vertical variation of Φ enters only the first-order (δ^1) momentum balance via the third-order electric field Φ_3. Furthermore, (2.26) gives

$$p_0 = p_0(x, y, t). \tag{2.28}$$

This independence of the pressure gradient and the electric body force in the z-direction in (2.25) suggests that the horizontal velocity $\boldsymbol{u}_0$ can be conveniently integrated to yield

$$\boldsymbol{u}_0 = \boldsymbol{U}_0 + \boldsymbol{u}_{eo_0}, \tag{2.29}$$

where

$$\boldsymbol{U}_o \equiv \left(\nabla_H p_o - \nabla_H^2 \Phi_o \nabla_H \Phi_o \right) \frac{(z^2 - 1)}{2} \tag{2.30}$$

is the internally generated flow, and we have applied the boundary condition (2.22) to the leading order.

We define a depth-averaging action as

$$\bar{f} \equiv \tfrac{1}{2} \int_{-1}^{1} f \, \mathrm{d}z. \tag{2.31}$$

When this action is applied to the velocity fields (2.29), (2.30), we obtain

$$\bar{\boldsymbol{u}}_0 = \bar{\boldsymbol{U}}_0 + \boldsymbol{u}_{eo_0}, \tag{2.32}$$

$$\bar{\boldsymbol{U}}_0 = -\tfrac{1}{3}\left(\nabla_H p_0 - \nabla_H^2 \Phi_0 \nabla_H \Phi_0 \right). \tag{2.33}$$

Now in terms of the depth-averaged flow fields $\bar{\boldsymbol{u}}_0$ and $\bar{\boldsymbol{U}}_0$, $\boldsymbol{u}_0$ can be re-expressed as

$$\boldsymbol{u}_0 = \bar{\boldsymbol{u}}_0 + \bar{\boldsymbol{U}}_0\left(\tfrac{1}{2} - \tfrac{3}{2}z^2\right). \tag{2.34}$$

Note that the parabolic velocity profile in (2.34) can induce a dispersion effect on the conductivity field as we will show in §2.3.

Next we consider the continuity equation (2.24); depth-averaging and considering that $w(z = \pm 1) = 0$, we obtain

$$\nabla_H \cdot \bar{\boldsymbol{u}}_0 = 0. \tag{2.35}$$

Equation (2.24) can also be integrated in the z-direction, making use of (2.34), to obtain the vertical velocity w_0 as

$$w_0 = (\nabla_H \cdot \bar{U}_0)\left(\frac{z^3}{2} - \frac{z}{2}\right). \tag{2.36}$$

The higher-order depth-averaged velocity fields may be obtained by performing the asymptotic analysis as well as the integration and depth-averaging actions to higher orders in δ. The procedure is lengthy but straightforward and we give the details in Appendix A.

With the evolution equation for the depth-averaged velocity field at different orders, we may now reconstruct the evolution equation for the total depth-averaged velocity $\bar{u}$ (Ghosal 2003), which we define as

$$\bar{u}(x, y) \equiv \bar{u}_0 + \delta\bar{u}_1 + \delta^2\bar{u}_2, \tag{2.37}$$

neglecting higher-order terms. We multiply (A 6) by δ, (A 7) by δ^2 and add to (2.32) to obtain

$$Re_d\delta\left(\frac{\partial\bar{u}}{\partial t} + \bar{u}\cdot\nabla_H\bar{u}\right) = -\nabla_H\bar{p} + \nabla_H^2\bar{\Phi}\nabla_H\bar{\Phi} - 3(\bar{u} - u_{eo}) + \delta^2\nabla_H^2\bar{u}. \tag{2.38}$$

Here $\bar{p}$, $\bar{\Phi}$ and u_{eo} are all reconstructed up to δ^2 in a similar manner using (2.23), and in arriving at (2.38) we have arbitrarily added or dropped terms of $o(\delta^2)$ without losing the second-order asymptotic consistency. This equation is similar to the DBF equation in porous media flow (Vafai & Tien 1981; Liu & Masliyah 1996). A linear version used for convective instability analysis has been introduced in a heuristic way in Chen *et al.* (2005). Note that in order to arrive at the final DBF form in (2.38), we have dropped additional terms in (A 6) and (A 7) (for $\bar{u}_1$ and $\bar{u}_2$, respectively). In principle, these terms can be incorporated into (2.38) in a straightforward manner, such that the final equation is rigorously second order in δ. However, we find such a formulation is cumbersome and impractical when implemented for numerical simulations, and we simplify the equations following the standard DBF form instead. Such an *ad hoc* simplification is nonetheless justified when we compare the DBF model with a direct non-depth-averaged model simulation as shown below. Further details on the simplification are presented in Appendix A.

Finally, because the divergence-free condition is satisfied at all orders ((2.35), (A 8) and (A 9)), $\bar{u}$ also satisfy the continuity equation

$$\nabla_H \cdot \bar{u} = 0. \tag{2.39}$$

2.3. *Conductivity field*

The conductivity field obeys the convective–diffusive equation (2.12). Naturally, for the thin channel that we are interested in with a parabolic velocity distribution such as (2.34), we would expect a dispersion effect similar to the Taylor–Aris type (Probstein 1994; Stone & Brenner 1999; Ghosal 2003). The asymptotic analysis on the conductivity equation yields this result.

The zeroth-order balance of (2.12) is simply

$$\frac{\partial^2\sigma_0}{\partial z^2} = 0. \tag{2.40}$$

This equation suggests that $\sigma_0 = \sigma_0(x, y, t)$, taking into account boundary condition (2.6). At the δ^1-order, we have

$$Pe_d\left(\frac{\partial \sigma_0}{\partial t} + \boldsymbol{u}_0 \cdot \nabla_H \sigma_0\right) = \frac{\partial^2 \sigma_1}{\partial z^2}. \tag{2.41}$$

When (2.41) is depth-averaged, with $\partial \sigma_1/\partial z = 0$ at $z = \pm 1$, we obtain an evolution equation for σ_0 as

$$\frac{\partial \sigma_0}{\partial t} + \bar{\boldsymbol{u}}_0 \cdot \nabla_H \sigma_0 = 0. \tag{2.42}$$

Note that we have taken into consideration that $\bar{w}_0 = 0$ since w_0 is an odd function in z. Now because we are equipped with the z-dependence of $\boldsymbol{u}_0$ (equation (2.34)), and considering that σ_0 is not a function of z, (2.41) can be integrated in the z-direction for σ_1 to obtain

$$\sigma_1 = \tfrac{1}{4} Pe_d(\bar{\boldsymbol{U}}_0 \cdot \nabla_H \sigma_0)\left(z^2 - \tfrac{1}{2}z^4\right) + C, \tag{2.43}$$

where C is an integration constant, and we have used (2.42) when evaluating the left-hand side of (2.41). Upon averaging, (2.43) yields

$$\bar{\sigma}_1 = \tfrac{7}{120} Pe_d(\bar{\boldsymbol{U}}_0 \cdot \nabla_H \sigma_0) + C, \tag{2.44}$$

with the aid of which we can re-express (2.43) as

$$\sigma_1 = \bar{\sigma}_1 + \tfrac{1}{4} Pe_d(\bar{\boldsymbol{U}}_0 \cdot \nabla_H \sigma_0)\left(-\tfrac{7}{30} + z^2 - \tfrac{1}{2}z^4\right). \tag{2.45}$$

The evolution equation for σ_1 is revealed only when we go to the δ^2-order balance of (2.12). The equation reads

$$Pe_d\left(\frac{\partial \sigma_1}{\partial t} + \boldsymbol{u}_1 \cdot \nabla_H \sigma_0 + \boldsymbol{u}_0 \cdot \nabla_H \sigma_1 + w_0\frac{\partial \sigma_1}{\partial z}\right) = \frac{\partial^2 \sigma_2}{\partial z^2} + \nabla_H^2 \sigma_0. \tag{2.46}$$

Here we have already taken into the consideration that $\partial \sigma_0/\partial z = 0$. The depth-averaging action with $\partial \sigma_2/\partial z = 0$ at $z = \pm 1$ yields an evolution equation for σ_1:

$$Pe_d\left(\frac{\partial \bar{\sigma}_1}{\partial t} + \bar{\boldsymbol{u}}_1 \cdot \nabla_H \sigma_0 + \overline{\boldsymbol{u}_0 \cdot \nabla_H \sigma_1} + \overline{w_0\frac{\partial \sigma_1}{\partial z}}\right) = \nabla_H^2 \sigma_0. \tag{2.47}$$

The convoluted averages can be evaluated using the expressions for $\boldsymbol{u}_0$, w_0 and σ_1, as given by (2.34), (2.36) and (2.45), respectively. The resulting equation reads

$$\frac{\partial \bar{\sigma}_1}{\partial t} + \bar{\boldsymbol{u}}_1 \cdot \nabla_H \sigma_0 + \bar{\boldsymbol{u}}_0 \cdot \nabla_H \bar{\sigma}_1 = \frac{1}{Pe_d}\nabla_H^2 \sigma_0 + \tfrac{2}{105} Pe_d[\bar{\boldsymbol{U}}_0 \cdot \nabla_H(\bar{\boldsymbol{U}}_0 \cdot \nabla_H \sigma_0)$$
$$+ (\nabla_H \cdot \bar{\boldsymbol{U}}_0)(\bar{\boldsymbol{U}}_0 \cdot \nabla_H \sigma_0)]. \tag{2.48}$$

Now similar to the construction of (2.38), we multiply (2.48) by δ, and add to (2.42) to obtain an evolution equation for $\bar{\sigma}$ up to the first order,

$$\frac{\partial \bar{\sigma}}{\partial t} + \bar{\boldsymbol{u}} \cdot \nabla_H \bar{\sigma} = \frac{\delta}{Pe_d}\left\{\nabla_H^2 \bar{\sigma} + \tfrac{2}{105} Pe_d^2\nabla_H \cdot [\bar{\boldsymbol{U}}(\bar{\boldsymbol{U}} \cdot \nabla_H \bar{\sigma})]\right\}, \tag{2.49}$$

where again all the total variables are reconstructed from their asymptotic expansions using (2.23), up to δ^1, and

$$\bar{\boldsymbol{U}} \equiv \bar{\boldsymbol{U}}_0 + \delta\bar{\boldsymbol{U}}_1 + \delta^2\bar{\boldsymbol{U}}_2 + \cdots = \bar{\boldsymbol{u}} - \boldsymbol{u}_{eo}. \tag{2.50}$$

In arriving at (2.49) we have arbitrarily added or dropped terms of $o(\delta)$ without losing the asymptotic consistency. The combination of the last two terms in (2.48)

yields the Taylor dispersion term $\nabla_H \cdot [\bar{U}(\bar{U} \cdot \nabla_H \bar{\sigma})]$ in conservative form in (2.49). Note that unlike the momentum equation (2.38) in which we included effects up to the second order, we shall study only the first-order effects in the conductivity equation. The reason for doing so (or rather, the reason for going to a higher-order analysis in the momentum equation) will be discussed in §3.

Equation (2.49) is a generalized two-dimensional Taylor-dispersion formulation. The right-hand-side term can be re-written as

$$\frac{\delta}{Pe_d} \nabla_H \cdot (\mathfrak{D} \nabla_H \bar{\sigma}), \tag{2.51}$$

where $\mathfrak{D}$ is a second-order tensor and defined as (in index form)

$$\mathfrak{D}_{ij} \equiv \delta_{ij} + \frac{2}{105} Pe_d^2 \bar{U}_i \bar{U}_j. \tag{2.52}$$

Here, δ_{ij} denotes the second-order unit tensor. In general $\mathfrak{D}$ is both heterogeneous and anisotropic, owing to the non-uniform dispersion velocity $\bar{U}$.

Note that in one-dimensional geometry (see (3.3) below) and when $\bar{U} = const$, (2.49) recovers the classical Taylor–Aris dispersion formulation, albeit with a different numerical coefficient (2/105) owing to the geometry. Equation (2.49) can also be simplified to (10) in Stone & Brenner (1999), when a cylindrically symmetric radial outflow (inflow) is considered.

When the depth-averaged conductivity is obtained from the evolution equation (2.49), the full three-dimensional conductivity field can be predicted (up to δ^1) using $\sigma = \sigma_0 + \delta\sigma_1$ and (2.45):

$$\sigma(x, y, z) = \bar{\sigma}(x, y) + \tfrac{1}{4} Pe_d \delta(\bar{U} \cdot \nabla_H \bar{\sigma})\left(-\tfrac{7}{30} + z^2 - \tfrac{1}{2}z^4\right). \tag{2.53}$$

2.4. *The Ohmic equation*

With the results from the previous section we are now ready to analyse the asymptotic structure of the electric potential which depends on the instantaneous conductivity field via the Ohmic current conservation law (2.13).

To the leading order, (2.13) gives

$$\frac{\partial}{\partial z}\left(\sigma_0 \frac{\partial \Phi_0}{\partial z}\right) = 0. \tag{2.54}$$

Considering that $\sigma_0 = \sigma_0(x, y)$ and the boundary condition (2.7), this equation suggests that

$$\partial \Phi_0 / \partial z = 0. \tag{2.55}$$

Using $\Phi_0 = \Phi_0(x, y)$, at the next order (δ^1) we obtain

$$\frac{\partial}{\partial z}\left(\sigma_0 \frac{\partial \Phi_1}{\partial z}\right) = 0. \tag{2.56}$$

We conclude similarly that

$$\partial \Phi_1 / \partial z = 0. \tag{2.57}$$

A governing equation for Φ_0 is revealed only at the asymptotic order of δ^2, namely

$$\nabla_H \cdot (\sigma_0 \nabla_H \Phi_0) + \frac{\partial}{\partial z}\left(\sigma_0 \frac{\partial \Phi_2}{\partial z}\right) = 0, \tag{2.58}$$

$$\nabla_H \cdot (\sigma_0 \nabla_H \Phi_0) = 0, \tag{2.59}$$

where (2.59) is derived from (2.58) via depth-averaging action and application of Neumann boundary conditions on Φ_2. We may also subtract (2.59) from (2.58) to yield

$$\partial \Phi_2 / \partial z = 0. \tag{2.60}$$

For our analysis we also require an equation for $\bar{\Phi}_1$, which is obtained at $O(\delta^3)$:

$$\nabla_H \cdot (\sigma_1 \nabla_H \Phi_0) + \nabla_H \cdot (\sigma_0 \nabla_H \Phi_1) + \frac{\partial}{\partial z}\left(\sigma_0 \frac{\partial \Phi_3}{\partial z}\right) = 0, \tag{2.61}$$

$$\nabla_H \cdot (\bar{\sigma}_1 \nabla_H \Phi_0) + \nabla_H \cdot (\sigma_0 \nabla_H \Phi_1) = 0. \tag{2.62}$$

The reconstruction process up to δ^1 (similar to that performed in §2.3) reveals the two-dimensional depth-averaged Ohmic equation as

$$\nabla_H \cdot (\bar{\sigma} \nabla_H \bar{\Phi}) = 0. \tag{2.63}$$

This equation preserves the form of the original three-dimensional equation (2.2).

2.5. *Summary of formulation*

Before we proceed, we summarize our equation system. We should keep in mind that these are the two-dimensional governing equations for depth-averaged quantities. The equations are:

$$\frac{\partial \bar{\sigma}}{\partial t} + \bar{u} \cdot \nabla_H \bar{\sigma} = \frac{1}{Ra_e}\left\{\nabla_H^2 \bar{\sigma} + \tfrac{2}{105} Ra_e^2 \delta^2 \nabla_H \cdot [\bar{U}(\bar{U} \cdot \nabla_H \bar{\sigma})]\right\}, \tag{2.64}$$

$$\bar{U} \equiv \bar{u} - u_{eo}, \quad u_{eo} \equiv -\frac{1}{R_v}\zeta \nabla_H \bar{\Phi}, \tag{2.65}$$

$$\nabla_H \cdot (\bar{\sigma} \nabla_H \bar{\Phi}) = 0, \tag{2.66}$$

$$\nabla_H \cdot \bar{u} = 0, \tag{2.67}$$

$$Re_H \delta^2 \left(\frac{\partial \bar{u}}{\partial t} + \bar{u} \cdot \nabla_H \bar{u}\right) = -\nabla_H \bar{p} + \nabla_H^2 \bar{\Phi} \nabla_H \bar{\Phi} - 3\bar{U} + \delta^2 \nabla_H^2 \bar{u}, \tag{2.68}$$

where

$$Ra_e \equiv Pe_d / \delta \tag{2.69}$$

is the electric Rayleigh number, which is similar to a Péclet number, but defined with the channel width H instead. We also use the in-plane Reynolds number

$$Re_H \equiv Re_d / \delta = U_{ev} H / \nu, \tag{2.70}$$

to be consistent with the new two-dimensional depth-averaged perspective. Note that when compared with (2.19), we have replaced Φ with the depth-averaged variable $\bar{\Phi}$. We will also replace the conductivity in the zeta potential relation (2.21) with the averaged variable $\bar{\sigma}$, namely, $\zeta = \bar{\sigma}(x, y)^{-n}$, $n = 0.33$. This approximation is asymptotically consistent and the justification is presented in Appendix B.

We compare our current equation set to the zeroth-order equation set that we derived and used in previous work (Storey *et al.* 2005):

$$\frac{\partial \bar{\sigma}}{\partial t} + \bar{u} \cdot \nabla_H \bar{\sigma} = \frac{1}{Ra_e}\nabla_H^2 \bar{\sigma}, \tag{2.71}$$

$$\nabla_H \cdot (\bar{\sigma} \nabla_H \bar{\Phi}) = 0, \tag{2.72}$$

$$\nabla_H \cdot \bar{u} = 0, \tag{2.73}$$

$$0 = -\nabla_H \bar{p} + \nabla_H^2 \bar{\Phi} \nabla_H \bar{\Phi} - 3\bar{U}, \qquad (2.74)$$

where $\bar{U}$ and $\boldsymbol{u}_{eo}$ have the same definitions as in (2.65).

The major contributions of the depth-averaged equations are the first-order correction for (Taylor–Aris-type) dispersion in the conductivity equation and the second-order-consistent momentum equations. Even though the zeroth-order equations have been demonstrated to provide excellent results in the linear analysis of electrokinetic flow instability (Chen *et al.* 2005; Storey *et al.* 2005), the higher-order effects are essential to a number of applications. As we shall see in the next section, the Taylor dispersion becomes significant when the conductivity gradients and electric field are colinear. Both Chen *et al.* (2005) and Storey *et al.* (2005) considered only the case where electric field and conductivity gradient were orthogonal. The in-plane diffusion in the momentum equation, albeit a small quantity compared with the major balances, provides crucial dissipation at high wavenumbers. The inclusion of this term (which is a second-order differential operator on $\bar{\boldsymbol{u}}$) also preserves the mathematical structure similar to the original Navier–Stokes equations, and reproduces boundary effects not captured by lower-order approximations (e.g. the electro-osmotic slip conditions at $y = \pm 1$ walls).

In §3, we shall compare numerical results from the new depth-averaged equations to direct numerical simulations and experimental data to validate the performance of the new model. In addition to validating the new equations, we will also elucidate the effects of both Taylor dispersion and in-plane momentum diffusion on the observed phenomena. In short, we will make detailed numerical comparisons between four models:

(*a*) (2.12)–(2.16) solved in three dimensions, hereinafter referred to as the 'direct numerical simulation' (DNS);

(*b*) (2.64)–(2.68), hereinafter referred to as the 'higher-order depth-averaged model';

(*c*) (2.65)–(2.68), but with (2.71) instead of (2.64) for conductivity, hereinafter referred to as the 'higher-order depth-averaged model without dispersion'; and

(*d*) (2.71)–(2.74), hereinafter referred to as the 'zeroth-order depth-averaged model' (although note that (2.71) does include a partial first-order term for molecular diffusion).

We emphasize that the model (*c*) is not derived from the asymptotic expansion; this model is presented only to clarify separately the physical effects of Taylor dispersion by omitting the associated term from the numerical simulation.

The above equations are studied via numerical simulation, details on the methods are provided in Appendix C.

3. Results

In this section, we consider two model problems to investigate the behaviour of the depth-averaged model and assess its validity. These two configurations are shown in figure 1.

In the Case I (figure 1*a*), we consider the electric field and the conductivity gradient to be coaxial. We investigate a small low-conductivity sample surrounded by a high-conductivity fluid in a periodic channel. This configuration has relevance to applications such as field amplified sample stacking (FASS) (Burgi & Chien 1991; Bharadwaj, Santiago & Mohammadi 2002), in which dispersion often leads to significant band-broadening effects (e.g. see Bharadwaj *et al.* 2002; Ghosal 2004; Bharadwaj & Santiago 2005).
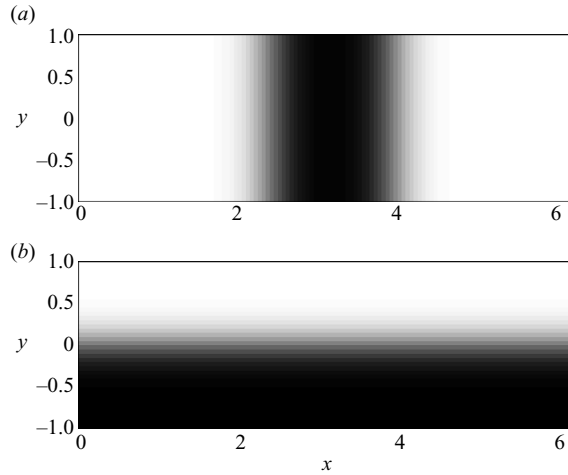
FIGURE 1. Basic flow configurations of study in this paper. (*a*) Case I, (*b*) Case II. In both cases the channel is thin in the *z*-direction (into the page) and the electric field points along the *x*-direction. Dark and light regions, respectively, denote low and high conductivity. The conductivity is initially assumed to be uniform in the *z*-direction.

In Case II (figure 1*b*), we consider the electric field and the conductivity gradients to be orthogonal. We revisit our previous work (Lin *et al.* 2004; Storey *et al.* 2005) and investigate a periodic shallow channel with the lower half-width filled with low-conductivity fluid and the upper half filled with high-conductivity fluid. Under this configuration the higher-order dispersion term (see (2.64) and (3.1) below) is only active when the flows become fully unstable (it plays no role in the initial growth of linearized disturbances).

While we will present our results in terms of dimensionless numbers, we base our parameter choice on typical experiments. For both of the cases the half-width of the channel is taken to be 500 μm, the channel half-depth is 50 μm (except for cases a, b, d and e presented in figures 3 and 10). The ratio of the high-to-low conductivity ratio in all cases is taken as 10:1. The physical parameters of the aqueous fluid are taken from experimental parameters summarized in table I of Lin *et al.* (2004).

3.1. *Case I: coaxial gradient*

We first study a simplified form of Case I to isolate and best illustrate the effect of the dispersion term, which, from (2.64), has the form

$$\tfrac{2}{105} Ra_e^2 \delta^2 \nabla_H \cdot [\bar{U}(\bar{U} \cdot \nabla_H \bar{\sigma})]. \tag{3.1}$$

At a local point (x_o, y_o), this dispersion term can be re-expressed as

$$\tfrac{2}{105} Ra_e^2 \delta^2 \frac{\partial}{\partial \boldsymbol{n}} \left(\bar{U}^2 \frac{\partial \bar{\sigma}}{\partial \boldsymbol{n}} \right), \tag{3.2}$$

where $\bar{U} \equiv |\bar{U}|$, and $\boldsymbol{n}$ is defined as the unit vector along the direction of the dispersion velocity vector $\bar{U}(x_o, y_o)$. The dispersion effect is maximal if $\bar{U}$ and $\nabla_H \bar{\sigma}$ point to the same direction, and minimal if they are at normal directions to each other. If we assume the flow is invariant in *y*, the conductivity equation is then simplified to
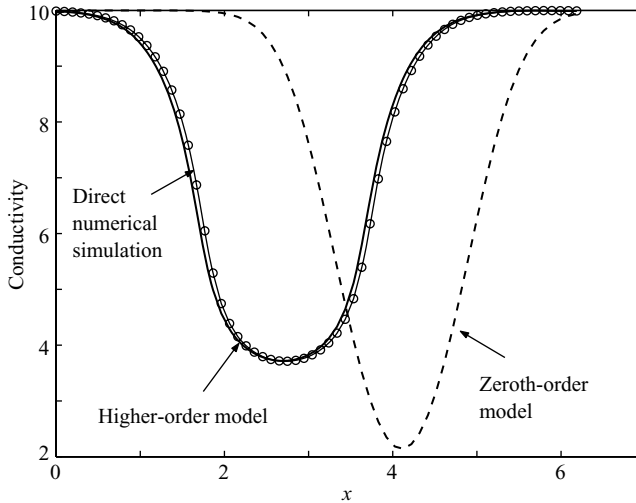
FIGURE 2. Shape of the axial conductivity profile as computed with three models for $Ra_e = 21.7$, $Re_H = 0.043$, $R_v = 2.8$ and $\delta = 0.1$. The higher-order depth-averaged model and the direct numerical simulation produce identical results. The zeroth-order depth-averaged model is inaccurate. The time of the snapshot is $t/t_o = 2$.

be one-dimensional:

$$\frac{\partial \bar{\sigma}}{\partial t} + \bar{u}\frac{\partial \bar{\sigma}}{\partial x} = \frac{1}{Ra_e}\left[\frac{\partial^2 \bar{\sigma}}{\partial x^2} + \frac{2}{105}Ra_e^2\delta^2\frac{\partial}{\partial x}\left(\bar{U}^2\frac{\partial \bar{\sigma}}{\partial x}\right)\right]. \tag{3.3}$$

Here the assumption of invariance in y is made only for simplicity and will be relaxed shortly. In this one-dimensional case, the Ohmic and the momentum equations become trivial. The former is

$$E = I/\bar{\sigma}, \tag{3.4}$$

where E is the electric field and I is the uniform constant ionic current, and the dispersion velocity $\bar{U}$ is simply given by

$$\bar{U} = \bar{u} - u_{eo} = \bar{u} - \frac{1}{R_v}\zeta(\bar{\sigma})E, \tag{3.5}$$

where $\bar{u}$ must be a constant to obey a constant mass flux. Equation (3.5) suggests that when the zeta potential depends on conductivity, the dispersion velocity $\bar{U}$ also becomes x-dependent. This non-uniformity in $\bar{U}$ directly contributes to the non-uniform dispersion of conductivity, via the second term on the right-hand-side of (3.3) (where $\bar{U}^2$ appears within the spatial derivative $\partial/\partial x$.) Equations similar to (3.3)–(3.5) can be found, for example, in Ghosal (2004), in the context of dispersion in (cylindrical) capillary electrophoresis devices.

In figure 2, we compare the axial conductivity profile at an instant in time as computed with the one-dimensional form of the higher-order depth-averaged model, the zeroth-order depth-averaged model and DNS. Following the y-invariance assumption, the DNS simulates the complete flow dynamics in the x- and z-directions. After the flow is computed via DNS, the result is depth-averaged for comparison. In figure 2, the electric field is taken to be $E_o = 5000\,\text{V}\,\text{m}^{-1}$, the channel length is $500\,\mu\text{m}$, the channel depth is $50\,\mu\text{m}$, and all electrolyte parameters are taken from Lin *et al.* (2004). These parameters correspond to $\delta = 0.1$, $Ra_e = 21.7$, $Re_H = 0.043$ and $R_v = 2.8$.
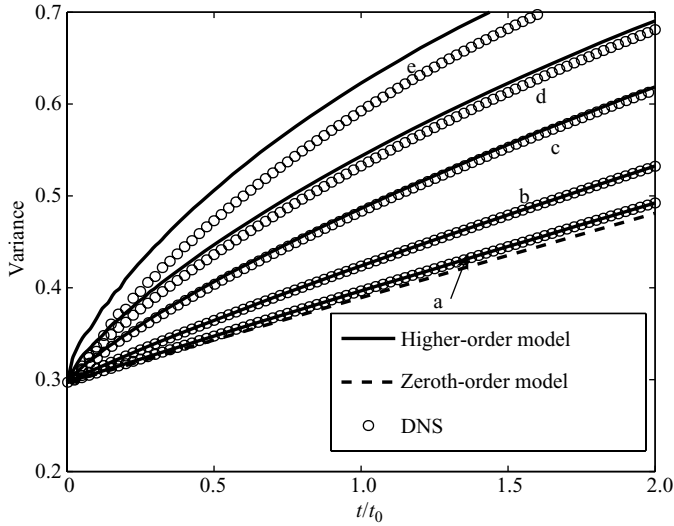
FIGURE 3. Variance of electrical conductivity σ as a function of time, computed from the three models, for $\delta = 0.02$, 0.05, 0.1, 0.14 and 0.2 (cases a–e, respectively). Other dimensionless parameters are identical for all the five cases, namely, $Ra_e = 21.7$, $Re_H = 0.043$ and $R_v = 2.8$. For small δ (case a) all three models converge. For moderate δ values (cases b–d) the higher-order model and DNS produce nearly identical results, which deviate from that from the zeroth-order model. The high-order model begins to lose accuracy when δ is further increased (case e). The time scale t_o here is taken to be that of case c, computed with (2.10), such that the variance is comparable on the same physical time scale.

We see excellent agreement between the higher-order depth-averaged model and the DNS. This figure shows both the effect of the advective dispersion in increasing the width of the sample region and in reducing the migration velocity of the peak, as is commonly known to occur in pressure-driven flows. The evolution computed from the zeroth-order depth-averaged model includes only molecular diffusion (see (2.71)) and provides the slowest rate at which the sample can spread.

Figure 3 shows the time evolution of sample variance computed from the three models at different channel depths. The variance, $\mathrm{Var}(\sigma)$, is computed with the formula

$$\mathrm{Var}(\sigma) = L_\sigma^2 = \int_0^{2\pi} \bar{\sigma}_{nc} x^2 \, \mathrm{d}x, \tag{3.6}$$

where L_σ characterizes the width of the sample plug, and $\bar{\sigma}_{nc}$ is normalized and re-centred at the computational domain from the conductivity profiles such as shown in figure 2. The five cases presented have the same parameters as figure 2, except that the channel depths are $d = 10$, 25, 50, 70 and $100\,\mu\mathrm{m}$, corresponding to $\delta = 0.02$, 0.05, 0.1, 0.14 and 0.2, respectively. The Rayleigh, Reynolds and R_v numbers are constants for all five cases, and are the same as those used in figure 2. We see that when δ is small (case a), the DNS, higher-order depth-averaged model, and zeroth-order depth-averaged model converge and are in close agreement. The convergence of the three models at small δ agrees with the asymptotic behaviour of the dispersion term in (3.3), where the dispersion term scales as $Ra_e^2 \delta^2$.

As δ increases, the DNS and higher-order model depart from the zeroth-order model (which does not depend on δ) indicating that dispersion is becoming important. For cases b–d the higher-order depth-averaged model and DNS remain in excellent
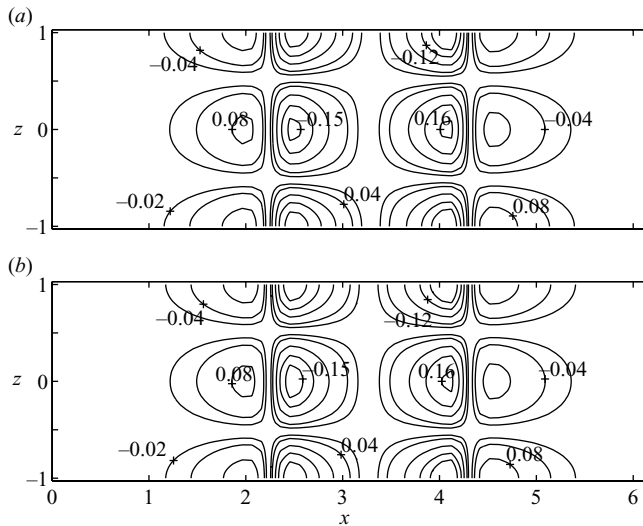
FIGURE 4. Contours of the deviation from the depth-averaged conductivity. (*a*) is from DNS and (*b*) is from (2.53). We find excellent agreement in the shape and magnitude of the disturbance fields computed from the two models. The depth-averaged, axial conductivity profile is shown in figure 2.

agreement. Visible deviation of the higher-order model from DNS is only seen for case e, $\delta = 0.2$. We tested numerous conditions and find that the higher-order model performs well under a significant range of parameters. The zeroth-order depth-averaged model consistently provides erroneous results at moderate values of δ and realistic operating conditions. This departure from the other two models is only natural, because dispersion behaves similarly to diffusion, such that the following scaling laws approximately apply:

$$\left.\begin{array}{ll} L_\sigma^2 \sim \dfrac{1}{Ra_e}\left(1 + \tfrac{2}{105}Ra_e^2\delta^2\bar{U}^2\right)t, & \text{higher-order model,} \\[2mm] L_\sigma^2 \sim \dfrac{1}{Ra_e}t, & \text{zeroth-order model,} \end{array}\right\} \tag{3.7}$$

Note that in figure 2, the higher-order and DNS models do not exhibit an exact linear behaviour owing to the non-uniform and changing dispersion velocity $\bar{U}$. Evidently for long enough time, the zeroth-order model is expected to deviate from the higher-order model (and the DNS) even for small $Ra_e^2\delta^2$ values.

In figure 4, we show a comparison of the conductivity fields along the shallow dimension of the channel (z) as computed from the DNS and predicted from the higher-order depth-averaged model using (2.53) and assuming y-invariance. The higher-order depth-averaged model accurately predicts the conductivity structure in the complete (x, z)-plane. Even though this higher-order model does not directly compute the variation of the conductivity and velocities in the z-direction, these results show that we can always use (2.53) to find the variation from the depth-averaged field. Again, while we show only a snapshot in figure 4, we find the result to be robust when checking other parameters and times.

We now relax our assumption of y-invariance and evaluate the two-dimensional behaviour of the governing equations (2.64)–(2.68), under the configuration of Case I. In these simulations, the channel is assumed to be periodic in x, solid boundaries are
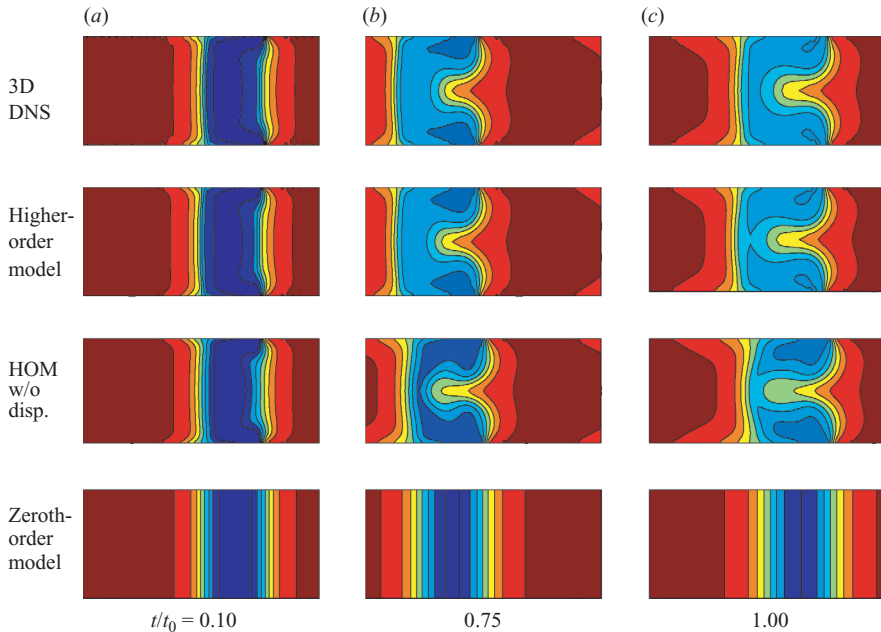
FIGURE 5. Conductivity field at various instances in time using four models. The (blue) low-conductivity sample plug is placed in a periodic channel (with $\delta = 0.1$) and allowed to travel in the x-direction and disperse within the channel. The comparison shows that the higher-order depth-averaged formulation produces near perfect agreement with the three-dimensional DNS. The utility of the DBF formulation is apparent as the boundary condition at $y = \pm 1$ induces significant conductivity variations in the y-direction. The time scale $t_o = 5.8$ s which is the same as in figure 3.

placed at $y = \pm 1$, and the channel aspect ratio is $\delta = 0.1$. We compare numerical results from the three-dimensional direct numerical simulation, the two-dimensional higher-order depth-averaged equations, the two-dimensional higher-order depth-averaged equations without dispersion (denoted 'HOM w/o disp.'), and the two-dimensional zeroth-order depth-averaged equations.

Figure 5 shows excellent agreement between the higher-order depth-averaged model and the three-dimensional DNS. Note that the DBF form of the momentum equation (which includes the δ^2-order in-plane viscous diffusion) supports the correct boundary conditions at $y = \pm 1$, and we can see from the example that this correction induces significant variations in the conductivity field across the spanwise direction of the channel. The same variation in electro-osmotic velocity that causes dispersion across the depth (z) direction occurs along the spanwise (y) direction as well. As described in Storey *et al.* (2005), the zeroth-order depth-averaged equations cannot support the correct boundary condition at $y = \pm 1$ as the overall order of the momentum equation has been reduced. The situation is analogous to using Euler equations in high-Reynolds-number flows; the equations are accurate in capturing the behaviour of the bulk, but the influence of the boundary condition can be very important. Just as neglecting the thin viscous boundary layer can prove detrimental in traditional fluid mechanics problems, we also find that proper treatment of all boundary effects are important in EK flows. We do find that as the channel depth is made smaller, the zeroth-order model becomes quite accurate in a manner similar to that shown
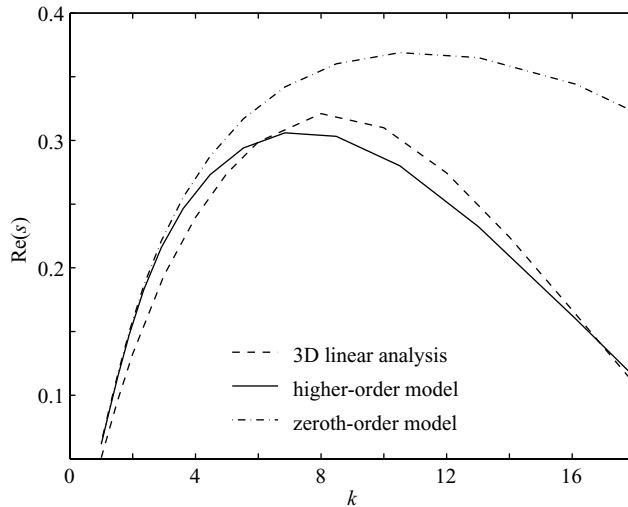
FIGURE 6. Real part of the growth rate versus the wavenumber for $Ra_e = 5000$, $Re_H = 10$, $R_v = \infty$ (no electro-osmotic flow) and $\delta = 0.1$, as computed with the three models. The higher-order depth-averaged model quenches the unphysical high-wavenumber growth and is in agreement with the three-dimensional analysis.

for one-dimensional flows in figure 3. Further advantages of the DBF form of the momentum equation will be discussed in § 3.2. See Vafai & Tien (1981) and Khaled & Vafai (2003) for porous media and biological tissue applications.

Note that the higher-order model without convective dispersion in the depth direction, although less accurate than the complete model at early times (figure 5a, b), provides good agreement with the three-dimensional DNS at later times (figure 5c). At later times, convective dispersion across the spanwise (y) direction is perhaps more important to the development of the conductivity field than dispersion across the depth (z) direction. The critical importance of spanwise dispersion in channels with high aspect ratios is discussed in detail by Ajdari, Bontoux & Stone (2005).

3.2. *Case II: orthogonal gradient*

We now turn to the second configuration (figure 1b) in which the conductivity gradient is orthogonal to the applied electric field, and we will focus on the study of electrokinetic instability (EKI).

We first perform a linear stability analysis to further demonstrate the advantage of the DBF momentum equation. The linearization of the higher-order depth-averaged equations, (2.64)–(2.68), follows the standard procedure assuming normal modes (see Lin *et al.* 2004; Storey *et al.* 2005 for details). For this particular configuration, because the base state for $\bar{U}$ is zero, the dispersion term vanishes as a higher-order effect in the linearized conductivity equation, and the only difference between the higher-order and zeroth-order models lies within the momentum equations. The linearization of the zeroth-order equations was presented in Storey *et al.* (2005). The higher-order depth-averaged model with and without dispersion are equivalent in this linear configuration.

Figure 6 plots the dimensionless growth rates as functions of wavenumber as computed from the three different models. The linear three-dimensional calculation was presented in Lin *et al.* (2004) and Storey *et al.* (2005). We find that the three models agree at low wavenumbers. However, at higher wavenumbers, the zeroth-order
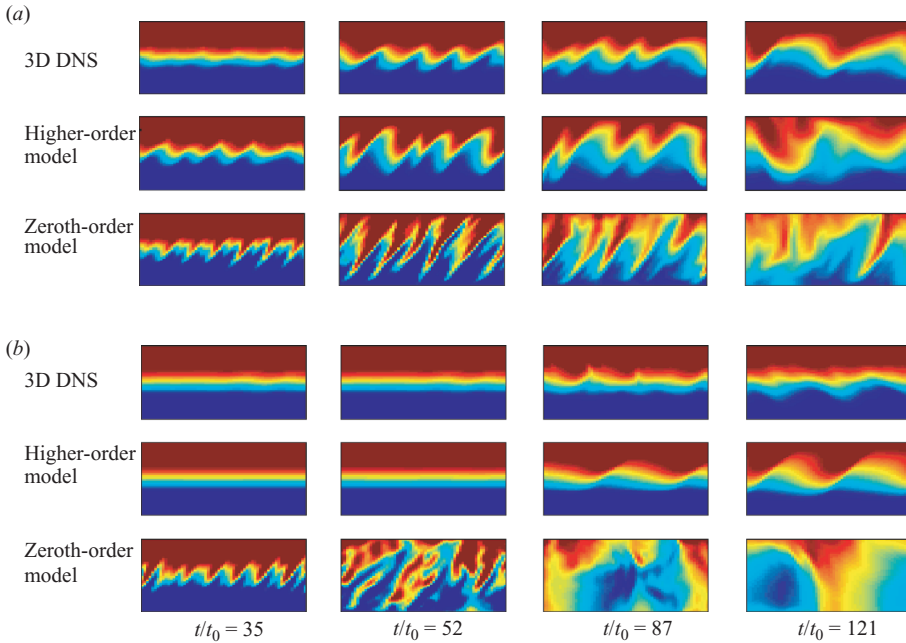
FIGURE 7. Snapshots of the conductivity field for three models at two different values of the electro-osmotic velocity. The high and low conductivity streams are denoted by red and blue, respectively. Each row is a different computation with time increasing from left to right. (*a*) $R_v = 12$ (lower electro-osmotic velocity), (*b*) $R_v = 3$ (higher electro-osmotic velocity), and the time scale $t_o = 0.06$ s. For three-dimensional DNS results, the three-dimensional conductivity field is first computed and then depth-averaged *a posteriori* to show the in-plane (x, y) evolution. In all cases, $\delta = 0.1$, $Ra_e = 2000$ and $Re_H = 4$.

depth-averaged model predicts unphysical growth rates, whereas the higher-order depth-averaged model quenches these growths in a manner consistent with the three-dimensional results. In figure 7, we observe that the nonlinear flow looks qualitatively different when these high-wavenumber motions are not quenched. Figure 6 is a representative example of what we observe under a wide range of conditions.

In the nonlinear regime, the higher-order depth-averaged model also provides superior results when compared with the zeroth-order model, as it captures the combined effects of the in-plane viscous diffusion and advective dispersion in the conductivity equation. First, the in-plane viscous diffusion in the higher-order model provides a natural damping mechanism which assures numerical stability of the nonlinear computation. In the zeroth-order model, the lack of damping at high wavenumbers causes these features to grow artificially; these motions must be either resolved or artificially damped when performing simulations. In order to simulate the zeroth-order equations successfully, we must include a hyperviscosity term on the conductivity equation (Boyd 1998; Pope 2000). Though better 'closure' models could be developed, we will show shortly that this use of hyperviscosity becomes unnecessary when we simply adopt the more physical higher-order depth-averaged model. Secondly, the dispersion effect in the conductivity equation, albeit a higher-order one in the linear regime, becomes significant as the dispersion velocity $\bar{U}$ grows along with the instability. This dispersion effect acts like an additional diffusion mechanism similar to that predicted by the classical Taylor–Aris theory (Probstein 1994).

In figure 7, we compute the nonlinear evolution of the EKI using three-dimensional DNS, the higher-order depth-averaged model, and the zeroth-order depth-averaged model. We show two cases of relatively high and low electro-osmotic velocity magnitudes. In all cases $\delta = 0.1$, $Ra_e = 2000$ and $Re_H = 4$; in figure 7(a) $R_v = 12$ and in figure 7(b) $R_v = 3$. To best illustrate the similarity and difference of the various model results, we elected to initialize each simulation with a collection of all the linearly unstable eigenfunctions in the range $0 < k < 7$ (see figure 6) with small amplitudes. These modes grow linearly at first, and nonlinear interactions occur as amplitudes increase. This initialization is convenient as it provides a repeatable condition across the three models. Note that the three-dimensional DNS typically requires an order of magnitude longer of computational time than the two-dimensional depth-averaged simulations for comparable in-plane (x, y) resolutions and integration time lengths.

Figure 7 demonstrates that the higher-order model provides good agreement when compared to the three-dimensional DNS. The advantage of the higher-order model over the zeroth-order model is more apparent at the higher electro-osmotic velocity $(R_v = 3)$, where dispersion effects are amplified when compared against the $R_v = 12$ case. The results also show clearly that the real nonlinear flow in EKI is much more damped than predicted by the zeroth-order model; the zeroth-order model over-predicts mixing rates and under-predicts the electric field threshold for instability. In observing the results from the zeroth-order model, the lack of damping at high wavenumbers is apparent in the conductivity fields. The higher-order model damps EKI dynamics via conductivity dispersion caused by velocity gradients along the depth (z) direction; this dispersion effect decreases the amplitude of and increases the width of instability waves.

Another way to assess quantitatively the superiority of the higher-order model over the zeroth-order model is to compare the maximum spanwise velocity. This velocity scales as the electroviscous velocity (Lin *et al.* 2004) and directly quantifies the strength of the instability. The results are shown in figure 8 for the same cases as discussed in figure 7. Similar to the presentation in figure 5, we also show v_{max} as computed from the higher-order model without the convective dispersion term. Again the complete higher-order model and the three-dimensional DNS show excellent agreement, whereas the zeroth-order model over-predicts v_{max} by an order of magnitude, and the higher-order model without convective dispersion over-predicts v_{max} by approximately 100 and 200%, for the cases of $R_v = 12$ and $R_v = 3$, respectively. The qualitative temporal development of the growth and subsequent decay of v_{max} are similar across the four models for the low electro-osmotic flow case (they both peak at about $t/t_o = 50$ and then decay). In the high electro-osmotic flow case, the higher-order models act to delay the development of the instability more significantly. We conclude that a higher-order depth-averaged formulation is required to model accurately the velocity field, mixing rate and nonlinear behaviour of EKI.

Finally, we briefly compare results from the higher-order model with experimental data in Lin *et al.* (2004); we use the same parameters as the results presented in that work (e.g. figure 2). The channel aspect ratio in this case is $\delta = 0.1$. Also, following our previous practice in the same work, we solve the convective diffusion equation of a low-diffusivity passive tracer to track the instability-stirred flow field. This passive tracer simulates the high-molecular-weight fluorescence marker used in the experiments, and facilitates comparison with experiments. The model shows good agreement with experiments (figure 9). At the lower applied field ($25\,000\,\text{V}\,\text{m}^{-1}$, corresponding to $Ra_e = 546.9$, $Re_H = 1.1$ and $R_v = 0.057$), both the experiment and the model simulation show only slight, sinuous and slowly growing interface disturbances.
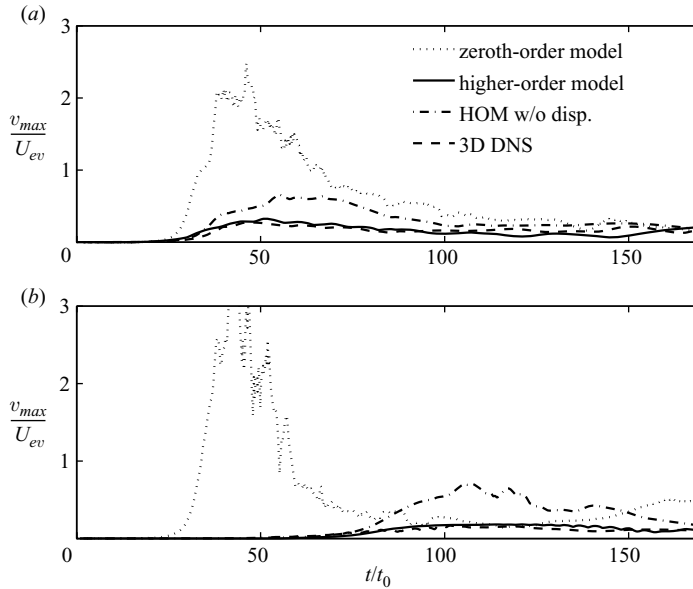
FIGURE 8. Comparison of maximum spanwise velocity. (a) $R_v = 12$ (b) $R_v = 3$. For the depth-averaged models, v_{max} is taken to be the maximum of the absolute spanwise velocity v in the (x, y)-plane at every instant of time. For three-dimensional DNS, the spanwise velocity field is first depth-averaged (*a posteriori*), and then the in-plane absolute value and maximum are obtained. For the cases shown here, the time and velocity scales are $t_o = 0.06$ s and $U_{ev} = 8$ mm s^{-1}, respectively. In all cases, $\delta = 0.1$, $Ra_e = 2000$ and $Re_H = 4$.
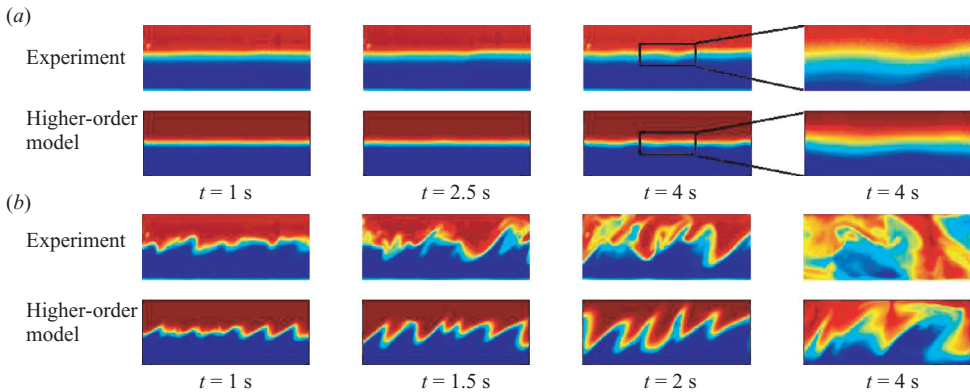

FIGURE 9. Comparison of higher-order depth-averaged model predictions with experimental data. Shown is the evolution of the conductivity field; high conductivity is denoted by red and low by blue. The parameters are taken from Lin *et al.* (2004). For both cases $\delta = 0.1$. (a) Applied field of $25\,000$ V m^{-1} in the streamwise x-direction ($Ra_e = 546.9$, $Re_H = 1.1$ and $R_v = 0.057$). (b) Applied field of $50\,000$ V m^{-1}($Ra_e = 2187.5$, $Re_H = 4.38$ and $R_v = 0.11$). Simulations demonstrate good agreement between model and experimental data. For the lower applied field of $25\,000$ V m^{-1} (a), the centre $1/3 \times 1/3$ regions for both experiment and simulation at time $t = 4$s have been magnified to show details of the slightly disturbed interfaces.

At the higher applied field of 50000 V m^{-1} ($Ra_e = 2187.5$, $Re_H = 4.4$ and $R_v = 0.11$), the experiment and simulation show similar dynamical evolutions, including a capture of the fastest growing wavenumber, and the rate at which the conductivity interfaces

break and evolve into the nonlinear rapidly stirred state. When compared with the purely two-dimensional simulations in Lin *et al.* (2004) (e.g. figures 6 and 7, in which the qualitative behaviour of the experiments is only reproduced at much lower applied electric fields), the higher-order depth-averaged model provides significantly improved predictions for EKI.

3.3. *A discussion on model validity*

Our asymptotic analysis has been developed based on combined lubrication (for the momentum equation) and Taylor–Aris dispersion (for the conductivity equation) theories. As previously mentioned, the established asymptotic orders from equations (2.12)–(2.16) are valid only when the constraints $Pe_d\delta \ll 1$ and $Re_d\delta \ll 1$ are satisfied. For example, if $Pe_d\delta \sim 1$ in (2.12), then the term on the left-hand side of the equation ($Pe_d\delta\,\mathrm{d}\sigma/\mathrm{d}t$) is of the same order as the $\partial^2\sigma/\partial z^2$ term on the right-hand side, violating the presumption that the latter is the leading term (cf. (2.40)). These constraints are conveniently understood using the following time-scale arguments:

$$Re_d\delta = \frac{\tau_\nu}{\tau_c} = \frac{d^2/\nu}{H/U} \ll 1, \qquad (3.8)$$

$$Pe_d\delta = \frac{\tau_d}{\tau_c} = \frac{d^2/D}{H/U} \ll 1, \qquad (3.9)$$

where τ_ν, τ_d denote the viscous and molecular diffusive time scales in the depth direction, respectively, τ_c is the in-plane convective time scale, and U is a characteristic dispersion velocity. (For significantly unstable electrokinetic flows, the characteristic dispersion velocity is simply the electroviscous velocity scale. For stable flows with significant conductivity gradient (e.g. in FASS), the correct dispersion velocity is typically the electro-osmotic velocity difference between low- and high-conductivity regions. To avoid any confusion, in the following we will compute the dispersion velocity directly and *a posteriori* from numerical simulation, for the estimate of any dimensionless parameters.) Equation (3.8) suggests that viscous diffusion is much faster than convection. In all our examples and in general microfluidic applications, Re_d is well below 0.1. Therefore, the Reynolds-number constraint is always well satisfied. The constraint on the Péclet number is more interesting and more detailed discussion is required.

Equation (3.9) suggests that molecular diffusion in the depth direction is much faster than in-plane convection. This condition must be satisfied such that any concentration gradient in the z-direction created by in-plane convection is quickly equilibrated by diffusion. This constraint is exactly the upper limit in the classical Taylor theory (Probstein 1994, p. 89):

$$Pe_d \ll 4H/d, \qquad (3.10)$$

where the factor of 4 is from the integration constant in (2.53) in the factor $Pe_d\delta/4$. However, there is a subtle difference between the classical Taylor–Aris theory and our two-dimensional dispersion model. In the former and given sufficient time, the sample will always spread enough such that the limit $L/d \gg Pe_d$ is reached, where L is the characteristic sample width. However, for flows where dispersion is driven by spanwise conductivity gradients, interface widths are limited by the channel width, H, and will not grow indefinitely (see figures 5, 7 and 9). For these cases, the limit (3.10) is effectively a limit on the instantaneous value of Pe_d.

We examine the above limit *a posteriori* for the results presented in figure 3. For reference, we also show the instantaneous Pe_d in addition to $Pe_d\delta$ in figure 10.
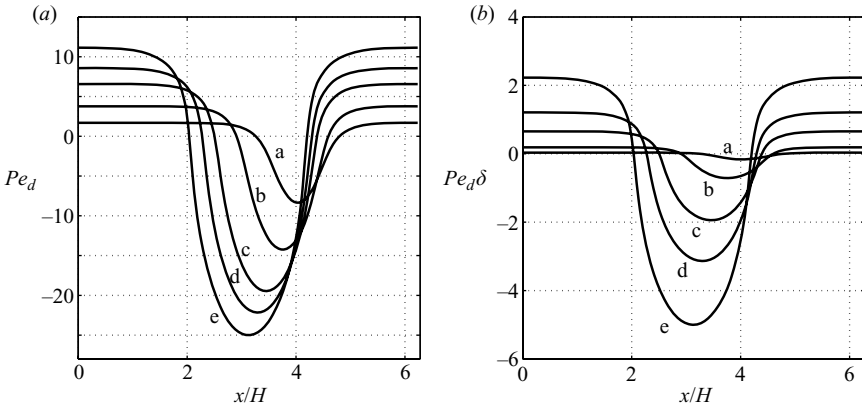
FIGURE 10. (*a*) Typical Pe_d and (*b*) $Pe_d\delta$ as a function of x for the 5 cases presented in figure 3: a, $\delta = 0.02$; b, $\delta = 0.05$; c, $\delta = 0.1$; d, $\delta = 0.14$ and e, $\delta = 0.2$. The time is taken at $t/t_o = 1$ for all 5 cases. Here the computed instantaneous dispersion velocity $\bar{U}(x)$ is used to compute both Pe_d and $Pe_d\delta$.

From (3.3), the relative importance of dispersion with respect to molecular diffusion increases along with Pe_d (note $Pe_d = Ra_e\delta$).

The variation in channel depth in the cases shown in figure 3 leads to variations in both Pe_d and $Pe_d\delta$. For all cases, Pe_d is calculated according to (2.18) with the instantaneous dispersion velocity $\bar{U}(x)$ at $t/t_o = 1$. As δ increases, Pe_d increases and Taylor dispersion plays an important role which can be captured by the higher-order model (cases b–d in figures 3 and 10). As δ increases further, $Pe_d\delta$ becomes large enough to exceed the criterion (3.10), and the higher-order depth-averaged model loses accuracy. A noticeable difference between DNS and the higher-order model appears only for case e, when $Pe_d\delta$ becomes moderately large and comparable to the value 4. These comparisons demonstrate that although theoretically (3.10) should be satisfied for model validity and accuracy, the model performs well even in the regime of $Pe_d\delta \sim 4$.

Similarly, we also analyse $Pe_d\delta$ for the cases presented in figures 5, 7 and 8. For this purpose we define both an averaged and a maximum dispersion velocity as

$$U_{ave} \equiv \frac{1}{A} \int_A |\bar{U}| \mathrm{d}A, \quad U_{max} \equiv max(|\bar{U}|), \tag{3.11}$$

where $|\bar{U}|$ is the magnitude of the internally generated velocity $\bar{U}$, computed *a posteriori* from the higher-order model, and the averaging action is performed over the entire computational domain A at each instant. The averaged and maximum parameters $Pe_d\delta_{ave}$ and $Pe_d\delta_{max}$ are then calculated. Figure 11 shows the time evolution of these parameters for the examples studied in figure 5, 7 and 8. For both cases, the flows are in a regime where Taylor dispersion plays a significant role, and $Pe_d\delta_{ave}$ are well within the range for which the dispersion theory is valid as demonstrated via figures 3 and 10. For all cases, $Pe_d\delta_{max}$ indicates greater values where the model may lose accuracy locally. However, these local deviations are not expected to cause a significant effect on model validity. The comparisons shown in figures 7 and 8 demonstrate that there is good agreement between our model and the three-dimensional DNS.
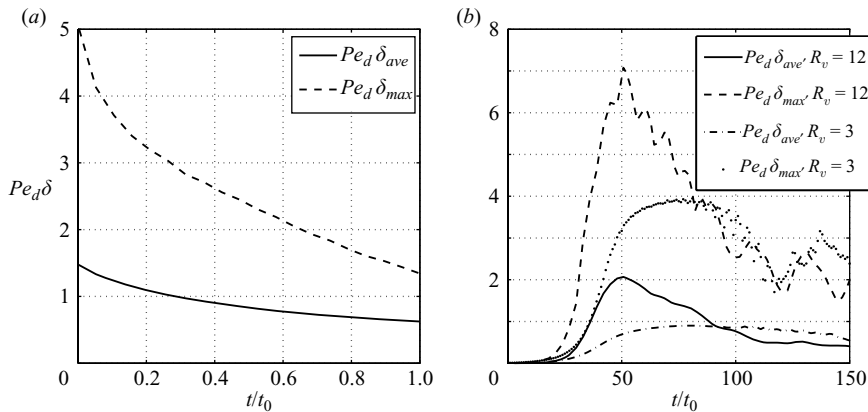
FIGURE 11. Time evolution of $Pe_d\delta_{ave}$ and $Pe_d\delta_{max}$. The curves correspond to (a) the case presented in figure 5, and (b) the $R_v = 12$ and $R_v = 3$ cases presented in figures 7 and 8. For all the cases $\delta = 0.1$.

Finally, in this work we focused on straight-channel geometry. Our model seems to capture the behaviour near the sidewalls (see e.g. figure 5). We speculate that this is due to the correct modelling of the velocity boundary conditions in the DBF momentum equation. As the velocity field converges to the electro-osmotic velocity on the channel sidewalls, dispersion effect also diminishes to zero. Although the quasi-two-dimensional assumption breaks down near the three-dimensional sidewalls, the modelled behaviour approximates the realistic physical situation. Caution must be taken when applying the model to geometries involving sharp corners (in the (x, y)-plane). For these cases, the electric field may become singular around the corner, and the flow field may become highly three-dimensional.

4. Conclusion

In this work, we have presented a depth-averaged model for general electrokinetic flows with heterogeneous conductivity configurations. Under this context, we have derived a Darcy–Brinkman–Forchheimer type of momentum equation, as well as a two-dimensional Taylor dispersion formula that can be also applied to general convective–diffusion phenomena other than in electrokinetic flow. We find that the higher-order depth-averaged model provides an excellent framework for analysing electrokinetic flows in shallow channels where the flow features are large compared to the depth of the channel. The model presented in this work provides excellent agreement with more computationally expensive direct numerical simulations of the three-dimensional governing equations. Though three-dimensional simulations are feasible, the depth-averaged framework provides a more convenient equation set; this is particularly true for design optimization efforts which require many trial simulations. The computational cost of the two-dimensional equations is significantly less than that of the three-dimensional formulation.

We found that an advective dispersion term in the conductivity equation accurately captures the convective–diffusion behaviour of the conductivity field in the depth direction, and provides an important spreading mechanism that is necessary for the accurate modelling of generalized EK flows in thin microchannels. Unlike the zeroth-order balance, the second-order DBF momentum equation captures boundary effects

and is not susceptible to errors in growth rate predictions at large wavenumbers. We have demonstrated with two examples that the current model is a valid framework for analysis, and makes reasonable predictions when compared with experimental results. We emphasize that the zeroth-order equations can be convenient in some instances for linear predictions and analysis, but taking the expansion to higher orders is the only realistic option when conducting nonlinear analysis or simulations.

The focus of this paper has been to develop the model framework and demonstrate via DNS that the higher-order depth-averaged model is appropriate for the study of generalized electrokinetic flows in thin microchannels with conductivity gradients. The model is accurate only if the assumptions behind the starting equation set are also valid. For example, in deriving the initial governing equations we assumed that charge relaxation was instantaneous, and that the electric double layers were very thin (see Lin *et al.* 2004 for details).

Throughout this paper we have analysed simple geometries (periodic channels) in order to facilitate comparisons between our model and DNS. Future work should involve further validating these depth-averaged equations against experimental data (including both FASS and EKI), modelling more complex geometries, and using the model to make optimal device design predictions.

Appendix A. Higher-order velocity fields

The calculation of higher-order velocity fields is straightforward, but algebraically involved. The first-order (δ^1) balance of the momentum equations yields

$$Re_d \left(\frac{\partial \boldsymbol{u}_0}{\partial t} + \boldsymbol{u}_0 \cdot \nabla_H \boldsymbol{u}_0 + w_0 \frac{\partial \boldsymbol{u}_0}{\partial z} \right) = -\nabla_H p_1 + \frac{\partial^2 \boldsymbol{u}_1}{\partial z^2} + \nabla_H^2 \Phi_1 \nabla_H \Phi_0$$

$$+ \nabla_H^2 \Phi_0 \nabla_H \Phi_1 + \frac{\partial^2 \Phi_3}{\partial z^2} \nabla_H \Phi_0, \quad \text{(A 1)}$$

$$\frac{\partial p_1}{\partial z} = 0. \quad \text{(A 2)}$$

We first note that (A 2) gives $p_1 = p_1(x, y, t)$. To integrate for $\boldsymbol{u}_1$, we also need an expression for Φ_3, which we derive from an integration of (2.61):

$$\Phi_3 = \frac{1}{48} Pe \left[\nabla_H (\bar{\boldsymbol{U}}_0 \cdot \nabla_H \ln \sigma_0) \cdot \nabla_H \Phi_0 \right] \left(\tfrac{7}{5} z^2 - z^4 + \tfrac{1}{5} z^6 \right). \quad \text{(A 3)}$$

In this integration, we have included the z-dependence of σ_1 from (2.45). With the aid of equations (2.34), (2.36) and (A 3), equation (A 1) can be integrated and then depth-averaged in the z-direction to yield

$$\bar{\boldsymbol{u}}_1 = Re_d \left[-\tfrac{1}{3} \left(\frac{\partial \bar{\boldsymbol{u}}_0}{\partial t} + \bar{\boldsymbol{u}}_0 \cdot \nabla_H \bar{\boldsymbol{u}}_0 \right) - \tfrac{1}{15} \left(\frac{\partial \bar{\boldsymbol{U}}_0}{\partial t} + \bar{\boldsymbol{U}}_0 \cdot \nabla_H \bar{\boldsymbol{u}}_0 + \bar{\boldsymbol{u}}_0 \cdot \nabla_H \bar{\boldsymbol{U}}_0 \right) \right.$$

$$\left. - \tfrac{1}{21} \bar{\boldsymbol{U}}_0 \cdot \nabla_H \bar{\boldsymbol{U}}_0 - \tfrac{2}{35} \bar{\boldsymbol{U}}_0 \left(\nabla_H \cdot \bar{\boldsymbol{U}}_0 \right) \right] - \tfrac{1}{3} \left(\nabla_H p_1 - \nabla_H^2 \Phi_1 \nabla_H \Phi_0 - \nabla_H^2 \Phi_0 \nabla_H \Phi_1 \right)$$

$$+ \tfrac{2}{315} Pe_d [\nabla_H (\bar{\boldsymbol{U}}_0 \cdot \nabla_H \ln \sigma_0) \cdot \nabla \Phi_0] \nabla \Phi_0 + \boldsymbol{u}_{eo_1}. \quad \text{(A 4)}$$

Although all the terms in the above expression can be incorporated in our final formulation (§2.2) in a straightforward manner, their numerical evaluation may become prohibitively expensive and impractical. Here, we use a simplified version instead:

$$\bar{u}_1 = Re_d \left[-\frac{1}{3} \left(\frac{\partial \bar{u}_0}{\partial t} + \bar{u}_0 \cdot \nabla_H \bar{u}_0 \right) \right] - \frac{1}{3} \left(\nabla_H p_1 - \nabla_H^2 \Phi_1 \nabla_H \Phi_0 - \nabla_H^2 \Phi_0 \nabla_H \Phi_0 \right) + u_{eo_1}, \quad \text{(A 5)}$$

or

$$Re_d \left(\frac{\partial \bar{u}_0}{\partial t} + \bar{u}_0 \cdot \nabla_H \bar{u}_0 \right) = -\nabla_H p_1 + \nabla_H^2 \Phi_1 \nabla_H \Phi_0 + \nabla_H^2 \Phi_0 \nabla_H \Phi_1 - 3(\bar{u}_1 - u_{eo_1}). \quad \text{(A 6)}$$

That is, we have neglected the 'higher-order' inertia as well as part of the first-order electric body force (led by the coefficient $Pe_d 2/315$). This *ad hoc* simplification is justified when we compare our numerical results with direct non-depth-averaged numerical simulations presented in §3. However, note that in general the leading coefficients of the dropped terms in (A 4) ($-1/15$, $-1/21$, $-2/35$ and $2/315$) are much smaller in magnitude when compared with those of the remaining terms ($-1/3$ and 1).

To arrive at a Darcy–Brinkman–Forchheimer type of equation (Vafai & Tien 1981; Liu & Masliyah 1996) we also require the δ^2 balance involving the evaluation of $\bar{u}_2$. The details of the derivation are not presented here, and we simply list the resulting equation as

$$Re_d \left(\frac{\partial \bar{u}_1}{\partial t} + \bar{u}_0 \cdot \nabla_H \bar{u}_1 + \bar{u}_1 \cdot \nabla_H \bar{u}_0 \right) = -\nabla_H \bar{p}_2 + \nabla_H^2 \Phi_0 \nabla_H \Phi_2$$
$$+ \nabla_H^2 \Phi_1 \nabla_H \Phi_1 + \nabla_H^2 \Phi_2 \nabla_H \Phi_0 - 3(\bar{u}_2 - u_{eo_2}) + \nabla_H^2 \bar{u}_0. \quad \text{(A 7)}$$

Similar to (A 6), we have also made *ad hoc* simplifications when arriving at (A 7).

Lastly, a simple verification shows that the continuity equation is satisfied at all orders, namely,

$$\nabla_H \cdot \bar{u}_1 = 0, \quad \text{(A 8)}$$
$$\nabla_H \cdot \bar{u}_2 = 0. \quad \text{(A 9)}$$

Appendix B. Zeta potential and electro-osmotic velocity

First, we note that when the zeta correlation (2.21) is used, the Helmholz–Smoluchowski formula does give a symmetric electro-osmotic velocity, i.e. u_{eo} $(z = +1) = u_{eo}(z = -1)$. This is simply because according to (2.53), (2.57), and (2.60), both σ and Φ are symmetric in z (at least to δ^1 for σ and δ^2 for Φ).

Further, when arriving at the final depth-averaged equation system, we have replaced Φ with $\bar{\Phi}$, and σ with $\bar{\sigma}$ in (2.65). For the electric field, this change is straightforward because Φ is z-independent up to δ^2, again according to (2.57) and (2.60). For conductivity, we can theoretically use (2.53) to evaluate the variable at the top and bottom of the channel. However, because the zeta potential has only a weak dependence on σ, $\zeta \sim \sigma^{-0.33}$, replacing the latter with $\bar{\sigma}$ results in an error of $\sim \delta/3$, which is almost second-order in magnitude. Therefore for convenience and simplicity of the formulation, we use $\bar{\sigma}$ instead. This simplification is justified by the favourable comparison of the depth–averaged model with direct numerical simulations (figures 2–4).

Note that (2.21) itself is an approximation: we have assumed that the zeta potential is identical on the top and bottom walls, depends only on the conductivity (electrolyte concentration), and that the response to changes in the latter is instantaneous. These restrictions are certainly not always satisfied. For example, the top and bottom channel walls may be composed of different material and thus have different chemical properties. In induced-charge electro-osmosis (Squires & Bazant 2004), the magnitude of the zeta potential depends also on the strength of the applied electric field. The surface charge may also have a significant response time to ion concentration (Raviv, Laurat & Klein 2002). Readers should carefully consider these restrictions for their applications.

Regardless of the specific forms of the electro-osmotic velocity, our analysis is valid, and the model is applicable as long as the difference in electro-osmotic velocity (from the top and bottom of the channel) is small when compared with the dispersion velocity. This criterion is briefly quantified in the following. (i) $|U| \gg |u_{eo}|$ is satisfied. This normally occurs in, e.g. EKI when internally generated flow field dominates (Lin *et al.* 2004). Under this situation u_{eo} may be completely ignored from the model system ($u_{eo}(z = \pm 1) = 0$) to good approximation. (ii) If $|U| \sim |u_{eo}|$ or $|U| \ll |u_{eo}|$, then

$$|u_{eo}(x, y, z = +1) - u_{eo}(x, y, z = -1)| \ll |U(x, y)| \qquad (B\,1)$$

must be satisfied. This criterion ensures the two-dimensionality of the electro-osmotic velocity.

Appendix C. Numerical methods

The equations presented in the previous section are solved using extensions of the numerical models developed in our previous work (Lin *et al.* 2004; Storey *et al.* 2005). All computations are based on Fourier–Chebyshev pseudospectral methods following some of the standard texts (Canuto *et al.* 1988; Boyd 2001; Peyret 2002). In all cases, we are interested in the temporal evolution of the flow, and we therefore assume that the channels are periodic in the x-direction. This assumption is made for simplicity and, if relaxed, the conclusions of this paper still hold.

For the two-dimensional depth-averaged simulations, we follow a velocity–pressure scheme as outlined in Peyret *et al.* (2002) for the Navier–Stokes equations. The nonlinear terms are computed in the usual pseudospectral manner; the nonlinear combinations are computed in physical space whereas the derivatives are computed in function space. The nonlinear electric body force and the convective terms are integrated forward using an Adams–Bashforth scheme. The viscous terms are integrated forward using a Crank–Nicolson scheme. The Stokes problem for the viscous terms and the Poisson equation for pressure are solved simultaneously using the influence matrix technique (Canuto 1988; Peyret *et al.* 2002). The algorithm that solves the Poisson equation for the pressure is also used in solving the current continuity equation to obtain the electric potential. Since the current continuity constraint is nonlinear, an iterative technique is employed.

The nonlinear dispersion term in the depth-averaged conductivity equations cannot be solved explicitly as it is a diffusive-like term and the resulting time-step stability constraint is costly. We implement a straightforward iterative technique to solve the conductivity dispersion and diffusive terms implicitly. We implement a standard iteration algorithm using the operator without the dispersion term as the pre-conditioning operator (Canuto 1988; Peyret *et al.* 2002).

The three-dimensional simulations use Chebyshev modes to represent the flow in the (y, z)-plane and Fourier modes are used in the x-direction. The time-advancement schemes are the same as in the two-dimensional case. The nonlinear terms are also treated in the same manner. All of the Helmholtz- and Poisson-type equations that occur in the formulation are solved using influence matrix techniques (Peyret *et al.* 2002). The viscous terms and continuity equation are coupled together through a predicted pressure projection method. The electric potential is solved iteratively since the current continuity equation is nonlinear.

REFERENCES

AJDARI, A., BONTOUX, N. & STONE, H. A. 2006 Hydrodynamic dispersion in narrow microchannels: the effect of cross-sectional shape. *Anal. Chem.* **78**, 387–392.

BHARADWAJ, R. & SANTIAGO, J. G. 2005 Dynamics of field amplified sample stacking. *J. Fluid Mech.* **543**, 57–92.

BHARADWAJ, R., SANTIAGO, J. G. & MOHAMMADI, B. 2002 Design and optimization of on-chip capillary electrophoresis. *Electrophoresis* **23**, 2729–2744.

BOYD, J. P. 1998 Two comments on filtering (artificial viscosity) for Chebyshev and Legendre spectral and spectral element methods: preserving boundary conditions and interpretation of the filter as diffusion. *J. Comput. Phys.* **143**, 283–288.

BOYD, J. P. 2001 *Chebyshev and Fourier Spectral Methods.* Dover.

BURGI, D. S. & CHIEN, R. L. 1991 Field amplified sample stacking (FASS): optimization in sample stacking for high performance capillary electrophoresis. *Anal. Chem.* **63**, 2042–2047.

CANUTO, C., HUSSAIN, M. Y., QUATERONI, A. & ZHANG, T. A. 1988 *Spectral Methods in Fluid Dynamics.* Springer.

CHEN, C.-H. & SANTIAGO, J. G. 2002 Electrokinetic instability in high concentration gradient microflows. *Proc. IMECE-2002*, CD vol. **1**, 33563.

CHEN, C.-H., LIN, H., LELE, S. K. & SANTIAGO, J. G. 2005 Convective and absolute electrokinetic instability with conductivity gradients. *J. Fluid Mech.* **524**, 263–303.

KHALED, A.-R.A. & VAFAI, K. 2003 The role of porous media in modeling flow and heat transfer in biological tissues. *Intl J. Heat Mass Transfer* **46**, 4989–5003.

GHOSAL, S. 2003 The effect of wall interactions in capillary-zone electrophoresis. *J. Fluid Mech.* **491**, 385–400.

GHOSAL, S. 2004 Fluid mechanics of electroosmotic flow and its effect on band broadening in capillary electrophoresis. *Electrophoresis* **25**, 214–228.

HERR, A. E., MOLHO, J. I., DROUVALAKIS, K. A., MIKKELSEN, J. C., UTZ, P. J., SANTIAGO, J. G. & KENNY, T. W. 2003 On-chip coupling of isoelectric focusing and free solution electrophoresis for multi-dimensional separations. *Anal. Chem.* **75**(5), 1180–1187.

HOBURG, J. F. & MELCHER, J. R. 1976 Internal electrohydrodynamic instability and mixing of fluids with orthogonal field and conductivity gradients. *J. Fluid Mech.* **73**, 333–351.

LIN, H., STOREY, B. D., ODDY, M. H., CHEN, C.-H. & SANTIAGO, J. G. 2004 Instability of electrokinetic microchannel flows with conductivity gradients. *Phys. Fluids* **16**, 1922–1935.

LIU, S. & MASLIYAH, S. 1996 Single fluid flow in porous media. *Chem. Engng Commun.* **148–150**, 653–732.

ODDY M. H., SANTIAGO, J. G. & MIKKELSEN, J. C. 2001 Electrokinetic instability micromixing. *Anal. Chem.* **73**, 5822–5832.

PEYRET, R. 2002 *Spectral Methods for Incompressible Viscous Flow.* Springer.

POPE, S. 2000 *Turbulent Flows.* Cambridge University Press.

PROBSTEIN, R. F. 1994 *Physicochemical Hydrodynamics.* John Wiley.

RAVIV, U., LAURAT, P. & KLEIN, J. 2002 Time dependence of forces between mica surfaces in water and its relation to the release of surface ions. *J. Chem. Phys.* **116**(12), 5167–5172.

REYES, D. R., IOSSIFIDIS, D., AUROUX, P.-A. & MANZ, A. 2002 Micro total analysis systems. 1. Introduction, theory, and technology. *Anal. Chem.* **74**, 2623–2636.

SADR, R., YODA, M., ZHENG, Z. & CONLISK, A. T. 2004 An experimental study of electro-osmotic flow in rectangular microchannels. *J. Fluid Mech.* **506**, 357–367.

Squires, T. M. & Bazant, M. Z. 2004 Induced-charge electro-osmosis. *J. Fluid Mech.* **509**, 217–252.

Stone, H. A. & Brenner, H. 1999 Dispersion in flows with streamwise variations of mean velocity: radial flow. *Ind. Engng Chem. Res.* **38**, 851–854.

Storey, B. D., Tilley, B. S., Lin, H. & Santiago, J. G. 2005 Electrokinetic instabilities in thin microchannels. *Phys. Fluids* **17**, 018103.

Vafai, K. & Tien, C. L. 1981 Boundary and inertia effects on flow and heat transfer in porous media. *Intl J. Heat Mass Transfer* **24**, 195–203.

Yao, S., Hertzog, D. E., Zeng, S., Mikkelsen, J. C. & Santiago, J. G. 2003 Porous glass electroosmotic pumps: design and experiments. *J. Colloid Interface Sci.* **263**, 143–153.